Chemical Engineering Journal 472 (2023) 145138

Contents lists available at ScienceDirect

Chemical Engineering Journal

journal homepage: www.elsevier.com/locate/cej

Separation of alkane isomers in a hierarchically structured 3D-printed porous carbon monolith

Adriano Henrique [a,b,c,d,*], Hendryk Steldinger [e], Jose L. Diaz de Tuesta [a,b,f], Jan Gläsel [e], Alírio E. Rodrigues [c,d], Helder T. Gomes [a,b], Bastian J.M. Etzold [e,*], José A.C. Silva [a,b,*]

[a] Centro de Investigação de Montanha (CIMO), Instituto Politécnico de Bragança, Campus Santa Apolónia, 5300-253 Bragança, Portugal
[b] Laboratório Associado para a Sustentabilidade e Tecnologia em Regiões de Montanha (SusTEC), Instituto Politécnico de Bragança, Campus de Santa Apolónia, 5300-253 Bragança, Portugal
[c] LSRE-LCM - Laboratory of Separation and Reaction Engineering - Laboratory of Catalysis and Materials, Faculty of Engineering, University of Porto, Rua Dr. Roberto Frias, 4200-465 Porto, Portugal
[d] ALiCE - Laboratory in Chemical Engineering, Faculty of Engineering, University of Porto, Rua Dr. Roberto Frias, 4200-465 Porto, Portugal
[e] Technical University of Darmstadt, Department of Chemistry, Ernst-Berl-Institut für Technische und Makromolekulare Chemie, 64287 Darmstadt, Germany
[f] Department of Chemical and Environmental Technology, ESCET, Rey Juan Carlos University, 28933, Móstoles, Madrid, Spain

ARTICLE INFO

Keywords:
3D-printed carbon monoliths
C5/C6 alkane isomer separation
Fixed bed adsorption
Molecular sieving
Numerical modeling

ABSTRACT

Hierarchically structured 3D printed porous carbons monoliths, exhibiting cylinder structures composed of tetragonal cubic centered unit cells, were studied for their applicability in adsorptive pentane (C5) and hexane (C6) alkane isomers separation (linear/branched). Three materials of the same macroscopic shape were employed in the study, which varied in the micro- and mesoporosity by changing the final CO_2 activation step: non-activated and activated at 1133 K for 6 and 12 h, respectively. Fixed bed breakthrough experiments were conducted for C5/C6 isomer feed mixtures, covering 373, 423, and 473 K temperatures and total alkane partial pressure up to 50.0 kPa. Results demonstrated that the initial porosity for the non-activated monolith enables the complete separation of linear from their respective branched isomers (slightly adsorbed) via a near molecular sieving effect, showing the following sorption hierarchy order (nC6 > nC5) ⋙⋙ (2MP > 3MP > 23DMB ≈ iC5 > 22DMB). Regarding the CO_2-activated monoliths, both showed a completely different picture, being all the alkane isomers adsorbed (much higher loadings) following the sorption hierarchy order: nC6 > 3MP > 2MP > 23DMB > 22DMB > nC5 > iC5. These results indicate that besides enhancing the microporosity and available specific surface area, the pore sieving effect of branched alkanes is lost due to the pore widening during the CO_2 activation. The breakthrough data for the non-activated monolith is also numerically fitted with a convenient, dynamic adsorption model.

1. Introduction

Structuring adsorbent materials for optimal process efficiency and easy implementation in large-scale processes is a fundamental step in their way toward commercialization. Porous materials synthesized by different methods are mainly generated as fine particles as a powder, which must be transformed into well-shaped bodies prior to industrial use while preserving the intrinsic properties of the powder. Otherwise, the particulate scatters and contaminates the engineering facilities. Techniques for producing appropriate macro-structured geometric forms, namely granules, pellets, and beads, have been widely developed as a route for powder scale-up [1–10]. However, the frequent problems associated with using these shaped materials in packed bed systems when higher throughputs are required impose limitations in operating such processes at optimum energy consumption and overall system efficiency. Drawbacks include the considerable pressure drop at high gas velocities, mass transfer restrictions related to gas diffusion into and out of the adsorbents, and low mechanical/attrition resistance [11,12].

Motivated by that, there has been a significant effort to devise new strategies to yield structured adsorbents into other configurations that could overcome these issues of traditional packing systems. In this regard, the monolithic engineered geometry has gained a great deal of

* Corresponding authors at: Laboratório Associado para a Sustentabilidade e Tecnologia em Regiões de Montanha (LA SusTEC), Instituto Politécnico de Bragança, Campus de Santa Apolónia, 5300-253 Bragança, Portugal(Henrique, Silva).
E-mail addresses: adriano_henrique@ipb.pt (A. Henrique), bastian.etzold@tu-darmstadt.de (B.J.M. Etzold), jsilva@ipb.pt (J.A.C. Silva).

https://doi.org/10.1016/j.cej.2023.145138
Received 1 June 2023; Received in revised form 28 July 2023; Accepted 29 July 2023
Available online 31 July 2023

attention as an alternative way to manufacture adsorbent materials [13]. Monolithic contactors present a unique geometry configuration consisting of parallel channels (i.e., continuous body with identical channels), which do not impart resistance to fluid flow. Therefore, resulting in a uniform flow pattern associated with a lower pressure drop across the bed while offering enhanced mass and heat transfer characteristics [11,12]. Such well-designed robust contactors are structured materials in which the shape and the diameter of the parallel channels, the wall thickness, and their cell density are controllable [14].

Over the past few years, the 3D printing technology, also known as rapid prototyping or additive manufacturing, has raised considerable interest for manufacturing structured adsorbents. This technique allows the digital design of the material structure in a 3D computer-aided design (CAD) software attached to 3D printers [15,16]. The unique design flexibility associated with the diversity of printing methods characterizes 3D printing as a more efficient and powerful technology for fabricating structured materials than traditional extrusion processes.

Currently, most research works deal with the application of 3D-printed monoliths as adsorbents for CO_2 capture from air/enclosed environments or post-combustion flue gas. Structures made of different material classes, such as aminosilica [17] (PEI-, TEPA-, APS-silica), zeolites [14,18,19] (5A, 13X, SAPO-34, and ZSM-5), polymer-zeolites [20] (Torlon-zeolite 13X and Torlon-zeolite 5A), MOFs [21–25] (MOF-74 (Ni), UTSA-16, and amine-functionalized MIL-101), polymer-MOFs [26] (40HKUST-1@Torlon and MOF-74@Torlon), and activated carbons [27] have been reported. In addition, hybrid 3D-printed zeolitic/carbonaceous monolithic structures (zeolite 13X/AC and zeolite 13X/graphite) have also been developed [28,29]. Interesting outcomes were obtained, with most monolithic adsorbents displaying comparable CO_2 uptake and separation performance, fast adsorption kinetics, relative stability, and regenerability to their powder analogs.

So far, to the best of our knowledge, there is no literature data on the use of 3D monolithic adsorbents for separating complex alkane mixtures with industrial interest (e.g., C5 and C6 isomers for the direct industrial application regarding the octane upgrading of gasoline in Total Isomerization Processes (TIP)). The value of a particular C5/C6 alkane as a component in the gasoline pool is related to its research octane number (RON) assigned. The higher the RON is, the higher the fuel's resistance to auto-ignition [30]. In other words, the fuel's combustion proceeds as a smooth explosion instead of a self-ignite and rapid inefficient detonation. As a general remark, branched C5/C6 alkanes have a higher RON (HRON) than their corresponding normal isomers (Table S1, Supplementary Data). Therefore, converting low RON (LRON) linear alkanes (n-pentane (nC5) and n-hexane (nC6)) into their branched counterparts and their separation through TIP processes is an industrially relevant process [30,31]. To achieve HRON blends, their separation is performed using the molecular sieve zeolite 5A, generating a final branched isomerate product stream with an average RON of nearly 89 [31,32]. Currently, about 2.5 million barrels of alkanes in the C5 and C6 range are processed daily to produce HRON gasoline in TIP processes [30].

In this work, a series of 3D-printed carbon-based monoliths were studied as adsorbents of C5/C6 alkane isomers, aiming their separation into linear and branched ones under dynamic fixed bed adsorption conditions. The materials were synthesized through a novel flexible, fast, and reproducible 3D-printing technique recently developed by Steldinger et al. [33]. The method is built on stereographically (SLA) 3D printing of a porous polymer, which is then transformed into activated carbon by thermal treatment for obtaining hierarchically structured porous carbons with high final carbon yield and controlled porosity. This is promising for identifying optimal carbonaceous structures that can be applied to multiple fields in adsorption separation processes of chemical mixtures. In this study, the macroscopic shape resulting from 3D printing, as well as the μm sized transport pore structure, were kept constant, but the smallest scales of micro- and small mesopores were varied. Interestingly, a near molecular sieving effect for the C5/C6 branched alkanes, similar to that observed with the benchmark zeolite 5A, could be identified for one of the materials.

2. Experimental section

2.1. Synthesis of 3D-Printed Carbon-Based monoliths

The materials were synthesized following a procedure recently developed by Steldinger et al. [33,34]. Accordingly, it consists of 4 main steps, as shown in Fig. 1:

i. Resin preparation: in a typical 3D printing process, 100 mL of the resin was prepared with the following reagents: 35 mL of pentaerythritol tetraacrylate (PETA, containing 10–40% triacrylate, 350 ppm hydroquinone) and 35 mL of divinylbenzene (DVB, containing 20% ethylstyrene, 1000 ppm p-*tert*-butylcatechol) as monomers; 30 mL of bis(2-ethylhexyl) phthalate (DOctP, ≥ 98%) as porogen; 0.4 $mg.mL^{-1}$ of color agent sudan1 (≥95%), and 10 $mg.mL^{-1}$ of phenylbis(2,4,6-trimethylbenzoyl) phosphine oxide (BAPO, 97%) as initiator. All the reagents are from *Sigma Aldrich*, except the porogen DOctP purchased from *Alfa Aesar*. The monomers and porogen were mixed in a Schott bottle. Thereafter, the color agent and the initiator were added to the mixture and placed in an orbital shaker at 350 rpm until a homogeneous phase was achieved. The Schott bottle was enwrapped with aluminum foil to avoid starting the photopolymerization prematurely;
ii. Photopolymerization: for the resin photopolymerization, a digital light processing (DLP) based stereolithography printer (*Titan 2 HR, Kudo 3D)* was used. The setup was adjusted by introducing a blue light filter (Schott BG-3) between the DLP projector and the resin vat. The custom-made resin vat consisted of an aluminum frame with outer dimensions of 180 (width) × 220 (length) × 30 mm (height), leaving an inner space of 140 × 180 mm. A 125 μm thick fluorinated ethylene propylene (FEP) film was fixed on this frame with adhesive tape. The 3D printing process consists of sequential illumination to photopolymerize single layers, with the elevation of the build platform to detach the printed part from the resin vat. First, a single layer height of 4 mm was printed by illuminating the photoresin with a 30 × 0.5 mm rectangle image for 240 s, applying a lifting speed of 2 $mm.min^{-1}$ and lowering speed of 10 $mm.s^{-1}$. Subsequently, a lift height of 2 mm, illumination time of 75 s, lifting speed of 4 $mm.min^{-1}$, and lowering speed of 50 $mm.s^{-1}$ were employed for producing the open-cell structures;
iii. Porogen extraction: after the 3D printing, the polymer structure generated is operated in a soxhlet extractor (100 mL, without thimble) to remove the porogen DOctP and the color agent Sudan1. The extraction is processed at 373 K for 24 h, using acetone as solvent (>20 $mL.g^{-1}_{polymer}$). Afterward, the polymer was dried at 333 K overnight in an oven;
iv. Thermal treatment (oxygen stabilization, pyrolysis, and CO_2 activation): the last step consists of the thermal treatment of the extracted polymer structures at different temperatures and atmospheres in a tubular quartz glass furnace (*Carbolite Gero*). Initially, the 3D-printed polymer was oxidized in the synthetic air for 6 h at 573 K with a heating ramp of 10 $K.min^{-1}$ (with nitrogen). Then, the oxidized sample is pyrolysed under a nitrogen atmosphere at 1173 K for 0.3 h after heating at a rate of 3.3 $K.min^{-1}$. Finally, CO_2 activation was applied to increase the microporosity of the resulting carbonaceous structure after heating at a rate of 10 $K.min^{-1}$ (with nitrogen).

The digital design of the monolith was performed in the programming-based compiler OpenSCAD, with the material comprising 8 tetragonal cubic centered unit cells, with a unit cell diameter of 5.7 mm and a thread diameter of 2 mm (Fig. 2a). It is worth mentioning that with hollow structured materials, the gases during pyrolysis can evolve

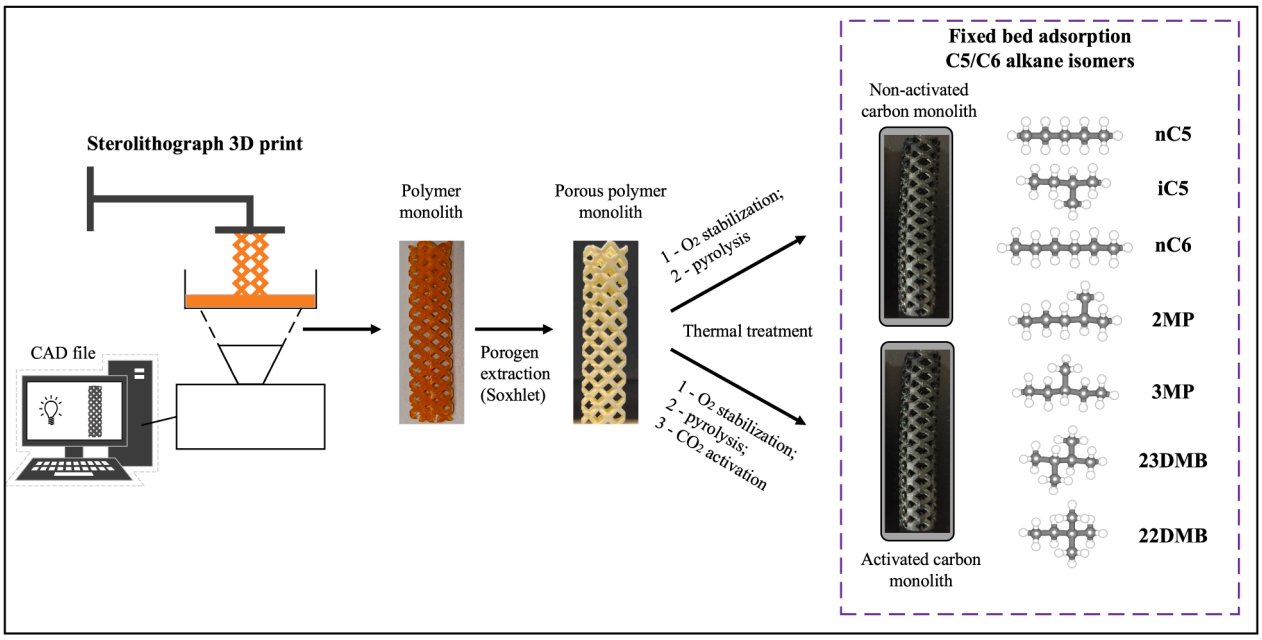

Fig. 1. Schematic overview of the 3D printing process of hierarchically structured porous carbon monoliths for studying the fixed bed adsorption of C5/C6 alkane isomers.

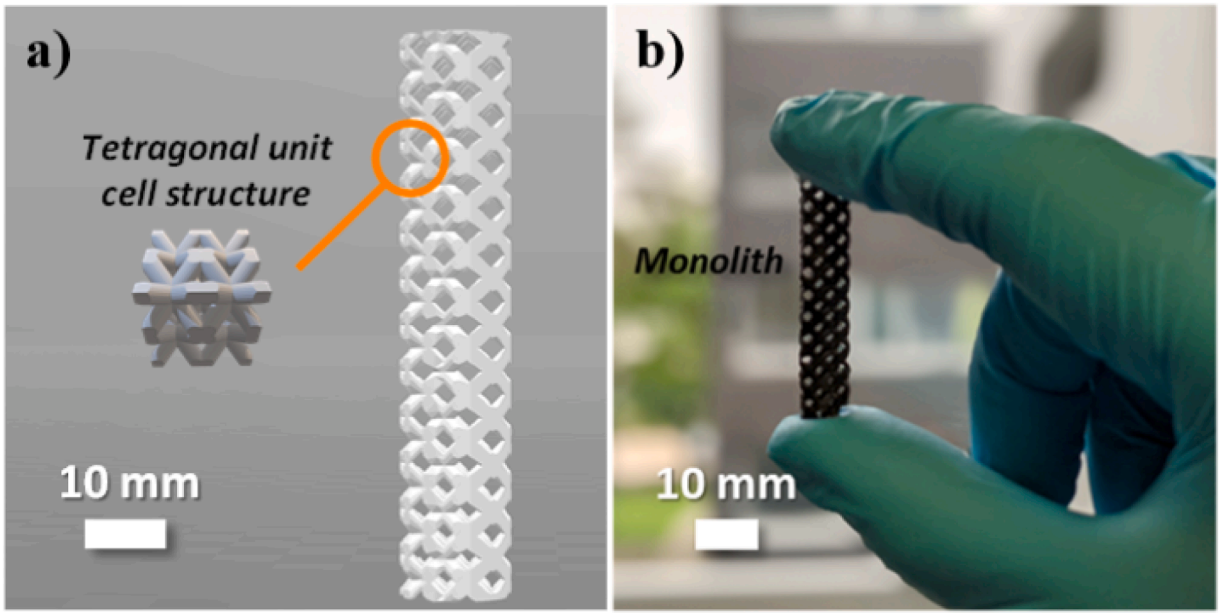

Fig. 2. Schematic view of 3D-printed monoliths: a) CAD structure used for the stereolithographic 3D printing, and b) Single piece of a monolith.

easily. For this study, three monoliths with different degrees of CO_2 activation were prepared: 1) non-activated (M1-pristine), 2) activated at 1133 K for 6 h (M2-CO_2_6h), and 3) activated at 1133 K for 12 h (M3-CO_2_12h) (Fig. 1, Fig. 2b, and Fig. S1 (Supplementary Data)).

2.2. Characterization of monoliths

Gas sorption measurements were conducted to give insight into the porosity of the 3D-printed monoliths. N_2 adsorption and desorption isotherms of the activated monoliths M2-CO_2_6h and M3-CO_2_12h were measured in a surface area analyzer (*BELSORP MAX II, Microtrac Retsch GmbH*) at a temperature of 77 K and a pressure range of 2.10^{-6}–1.10^{2} kPa. Beforehand, the samples (≈ 90 mg) were degassed at 523 K for 4 h under a fine vacuum. The specific surface area was calculated by applying the BET multi-point method considering five appropriate data points (S_{BET}), and the Quenched solid density functional theory for carbon with a combined slit- and cylindrical pore geometry (S_{QSDFT}). In addition, pore size distributions and the pore volume were also deduced by the QSDFT model (fitting errors < 0.2%, *VersaWin Vers. 1.0*). The characterization data for the monolith M1-pristine were taken from the works previously reported by Steldinger et al. [33,34].

2.3. Experimental fixed bed adsorption setup and procedure

The screening studies were performed in an experimental apparatus developed for measuring multicomponent breakthrough curves in a

fixed bed, which consists of three main sections: i) gas preparation, ii) adsorption, and iii) analytical section. In the gas preparation section (i), the carrier gas helium and the alkanes (in the liquid phase) are introduced into the system by a mass flow controller (helium) and a syringe pump (alkanes), respectively. Both run through a vaporizer before flowing into the adsorption column placed inside a preparative gas chromatograph, which has a precise, temperature-controlled oven that keeps the column at near isothermal conditions. The adsorption section (ii) consists of a stainless-steel column (i.d. 10 mm and length 120 mm) packed with the 3D-printed adsorbent material (as synthesized). The monolithic structures were wrapped with inert glass wool to avoid gas channeling through the fixed bed, and the column void end was filled with a short layer of small glass spheres. The outlet stream of the fixed bed is directed to the analytical section (iii), where a chromatograph equipped with a 6-way sampling valve delivered an aliquot of gas to a capillary column (with a 15 m length, 0.1 mm outside diameter and 0.1 μm poly(dimethyl sulfoxane) coating) every 1.5 min. Then, the component peaks are analyzed in a Flame Ionization Detector (FID). The equilibrium loading (amount adsorbed) is determined by integrating the concentration profiles of the breakthrough curves for each component. Detailed information on the system's characteristics and experimental procedure has already been reported elsewhere [35,36].

For the whole adsorption study, all C5/C6 alkanes were of analytical grade with 99+% purity. *Sigma Aldrich* supplied all hexane isomers (n-hexane (nC6), 2-methylpentane (2MP), 3-methylpentane (3MP), 2,2-dimethylbutane (22DMB) and 2,3-dimethylbutane (23DMB)) while *Riedel-de Haën* and *Fluka* supplied the pentane isomers, n-pentane (nC5) and *iso*-pentane (iC5), respectively.

2.4. Experimental description

The adsorption behavior of C5/C6 alkane isomers on the hierarchically structured 3D-printed porous carbons monoliths was evaluated through a series of breakthrough experiments. Equimolar septenary feed mixtures with the alkane isomers (nC5/iC5/nC6/2MP/3MP/23DMB/22DMB) were studied at three different temperatures, 373, 423, and 473 K, and total alkane partial pressure of 10, 25, and 50 kPa. All experiments were performed at a constant total pressure of 101.3 kPa, set by mixing the alkanes with helium. Complete information on the experimental conditions, including the flowrates of alkane mixture and helium, is given in Table S6 (Supplementary Data). The average RON of the product mixture leaving the adsorption column was calculated as a weighted average of the RONs of each component (Eq. S1, Supplementary Data).

3. Numerical section

3.1. Mathematical modeling

A general mathematical model has been developed to conveniently simulate (fit) the history profiles of the C5 and C6 alkanes observed in the breakthrough experiments. Dynamic fixed bed adsorption models are described with fundamental partial differential equations (PDEs), distributed over time and space according to the material and energy conservation laws for the components, coupled to their transport rate (kinetic mechanisms) and thermodynamic data (adsorption equilibrium isotherms). Considering this, the model equations are presented in Table S2 (Supplementary Data). Additional information about the dynamic mathematical model, including initial and boundary conditions, the correlations for estimating the transport parameters, and details of the numerical procedure applied to solve the PDÉs equations, is reported in Section S2 (Supplementary Data).

4. Results and discussion

4.1. N_2 Adsorption and desorption isotherms of 3D-Printed monoliths

Fig. 3 and Table 1 summarize the results of sorption characterization and the material's physical properties. As can be seen, the N_2 isotherms (Fig. 3a) for the three monoliths show a combination of type I and IV, according to the updated classification of the International Union of Pure and Applied Chemistry (IUPAC), pointing out the combined micro- and mesoporous character of these materials [37]. For microporous solids, the type I isotherm shows an almost vertical branch in the first region of the curve, which is related to enhanced adsorbent-adsorptive interactions in narrow pores, resulting in micropore filling. Indeed, Fig. 3a reveals that at very low relative pressures (p/p_0 between 2.10^{-8} to 5.10^{-2}), the N_2 adsorption progressively increases to 130, 190, and 260 $cm^3.g^{-1}$ for M1-pristine, M2-CO_2_6h, and M3-CO_2_12h, respectively. On the other hand, at higher relative pressures, hysteresis loops, which are generally associated with capillary condensation, are also visible for the three materials, characteristic of type IV isotherms typical of mesoporous solids. Based on their shapes, the hysteresis loops can be classified as H4, often found in micro-mesoporous carbons, and show a characteristic step down at relative pressure of around 0.45. Also, for M1-pristine, the hysteresis could not be fully closed, even for very long equilibration times, which is a sign of molecular sieving properties.

As explained above, the macroscopic size and shape of the monoliths are determined by the computer-designed structure, while on the nm level, the porosity can be varied through CO_2 activation conditions. By increasing the activation time at a temperature of 1133 K from 6 to 12 h, the material burn-off almost linearly scales from 13.6 to 26.3 wt% (Table 1). The partial oxidation of M2-CO_2_6h and M3-CO_2_12h led to a distinct rise of the N_2 uptake in the low-pressure region of the adsorption branch ($p/p_0 < 5.10^{-2}$) compared to M1-pristine, indicating the creation of additional microporosity. The prolonged activation time equally increases the specific surface area and pore volume of M3-CO_2_12h (S_{QSDFT}: 1307 $m^2.g^{-1}$; 0.52 $cm^3.g^{-1}$) compared to M2-CO_2_6h (S_{QSDFT}: 1048 $m^2.g^{-1}$; 0.39 $cm^3.g^{-1}$). Moreover, according to the cumulative pore volume distributions shown in Fig. 3b, the most significant gain in M2-CO_2_6h and M3-CO_2_12h can be attributed to micropores with a diameter of<1.5 nm. Thus, the CO_2 activation process can be utilized as a viable tool to introduce additional micropores without excessively altering the mesoporosity. Table 1 also reports the bulk density for each monolith (important for the design of industrial adsorption columns), which varies from 0.56 $g.cm^{-3}$ (M1-pristine) to 0.39 $g.cm^{-3}$ (M3-CO2_12h). These values fall in the same range of commercial activated carbon (0.25 to 0.75 $g.cm^{-3}$) [38] and also compare to the one of benchmark zeolite 5A (around 0.6 $g.cm^{-3}$) [39], especially M1-pristine. Additional information on the physical properties of the 3D-printed monoliths, including mechanical load tests, can be found in previous works [33,34].

4.2. Multicomponent fixed bed adsorption of C5 and C6 isomers in 3D-Printed monoliths

Fig. 4 shows the breakthrough curves for a septenary equimolar mixture of C5/C6 alkane isomers fed to the fixed bed column at the temperature of 373 K and total alkane partial pressure of 50.0 kPa. The 3D-printed monoliths are expressed in the panels: a) M1-pristine, b) M2-CO_2_6h, and c) M3-CO_2_12h. For a direct comparison between the monoliths, the data are plotted in terms of the ratio of the normalized molar fraction of each alkane as a function of the total molar amount fed per unit mass of adsorbent. The average RON of the product mixture leaving the column is also plotted in the figures (right y-axis).

As can be seen, and remarkably, the disclosed breakthrough curves completely differ between the monoliths before and after the CO_2 activation process. For M1-pristine (Fig. 4a), the adsorption hierarchy order is as follows: (nC6 > nC5) ⋙⋙ (2MP > 3MP > 23DMB ≈ iC5 >

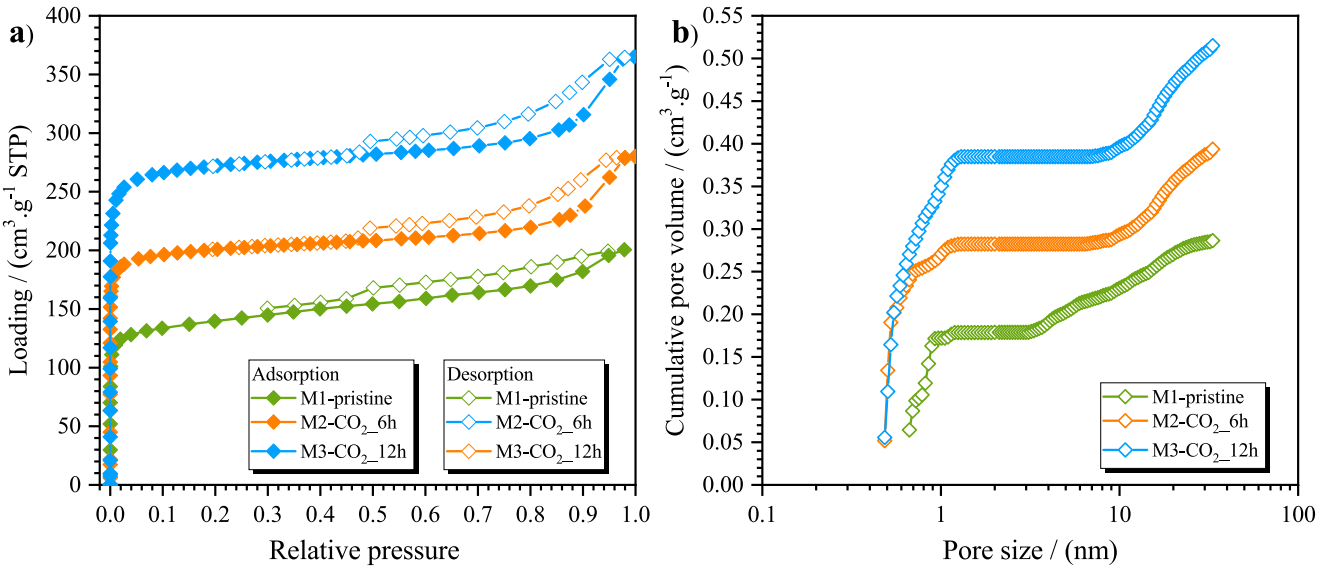

Fig. 3. N_2 sorption measurements at 77 K of 3D-printed monoliths: a) Adsorption and desorption isotherms (a logarithm plot is given in Figure S2), and b) Cumulative pore volume distribution.

Table 1
Physical and textural properties of 3D-printed monoliths determined by N_2 sorption measurements.

Physical properties				
		M1-pristine*	M2-CO$_2$_6h*	M3-CO$_2$_12h*
Burn-off	(%)	–	13.6	26.3
Total mass (dry)	(g)	2.36	1.94	1.66
Total length	(mm)	84.0	84.0	84.0
Diameter	(mm)	8.00	8.00	8.00
Bulk density$^+$	(g.cm^{-3})	0.56	0.46	0.39
N_2 sorption data				
S_{BET}	(m^2.g^{-1})	538	805	1078
S_{QSDFT}	(m^2.g^{-1})	536	1048	1307
Total pore volume	(cm^3.g^{-1})	0.29	0.39	0.52

* Each monolith consists of two individual pieces resulting in the respective total mass and length;
$^+$ Calculated by the ratio of total mass (dry) over the monolith volume.

22DMB), being clear the ability of the material to separate linear from branched alkane isomers via a near molecular sieving mechanism, similar to the one observed in the benchmark molecular sieve zeolite 5A [31,32]. The HRON isomers 22DMB/iC5/23DMB elute from the column first, at the very beginning of the experiments, closely followed by the mono-branched hexanes 3MP and 2MP. All the branched alkanes practically reach the feed flowrate at a total molar amount fed of 0.5 mol.kg^{-1}, while the linear nC5 and nC6 start their breakthrough only at 1.5 and 2.0 mol.kg^{-1}, respectively. Regarding the RON values, a plateau at 89 is reached when all branched alkanes leave the column separated from the linear ones. To the best of our knowledge, the ability to separate C5/C6 alkane isomers feeds into fractions of linear and branched ones has never been reported to such an extent before in any porous solid carbonaceous materials.

The separation arises due to the micropore morphology and connectivity of the monolithic structure. Generally, two different types of micropores can be present in the material, being defined as pores accessible by all species and pores with restricted access (molecular sieving character) [40]. Micropores with narrow openings (pore mouth), which cannot be easily accessible, are expected to be present next to the pores accessible by all species, which are well-connected and quickly filled. Consequently, the entrance to the pores with molecular sieving properties is narrow enough to allow the passage of the linear molecules, apparently under some diffusional limitations, while getting impassable by their branched counterparts. Therefore, ultimately resulting in the size-selective separation. Regarding the mixture loading, one can see that 77.4% of its value (0.86 mol.kg^{-1}, Table S6, Supplementary Data) corresponds to the adsorption of nC5 and nC6. This indicates a substantially higher volume in the micropores with molecular sieving character, which might explain the small amounts of branched alkanes filled in the pores accessible by all species.

These findings reveal that not only materials with a uniform pore size distribution can show molecular sieving properties. As demonstrated in Fig. 3b, M1-pristine has a broad pore size distribution; however, the smallest pores, as connection points as well as the so-called pore mouths, are important features that induce molecular sieving effects in such a pore network. The advantage of heterogeneous networks is that the transport is not breaking down fully due to single-file diffusion. Moreover, the non-closed hysteresis in Fig. 3a is a sign of such a pore architecture, which indicates that the pyrolysis leads to such molecular sieves where the pore mouths are essential.

On the other hand, both CO_2-activated monoliths (M2-CO$_2$_6h and M3-CO$_2$_12h) do not exhibit such a size-exclusion separation. Fig. 4b and c reveals that all alkane isomers were significantly adsorbed, with most of them practically showing a simultaneous elution at a total molar amount fed of 2.0 and 3.0 mol.kg^{-1}, respectively. Moreover, there is a change in the elution order of the components, with the C5 isomers leaving the column first. Also, a shift between the mono-branched hexanes 2MP and 3MP is seen. Therefore, for both monoliths M2-CO$_2$_6h and M3-CO$_2$_12h, the adsorption hierarchy is equal to nC6 > 3MP > 2MP > 23DMB > 22DMB > nC5 > iC5, consistent with the normal boiling point order of the components, showing a pure thermodynamic adsorption separation trend. This is also clearly highlighted by the shape of the breakthrough curves where a roll-up phenomenon is observed, typical of thermodynamically equilibrium competition for the sorption of species with different affinities in fixed bed columns. The least adsorbed components with weaker affinities are pushed out from the adsorbent by the ones with stronger affinities, and therefore their concentration sequentially rises above the feed. In the case of iC5 in M3-CO$_2$_12h, the rise in concentration can even quadruplicate the one of the feed, clearly indicating the strong competition for sorption inside the monolithic structure.

The comparison of the mixture loadings (Table S6, Supplementary Data) calculated from the integration of the history profiles of each component shown in Fig. 4 reveals that the adsorption uptake achieved

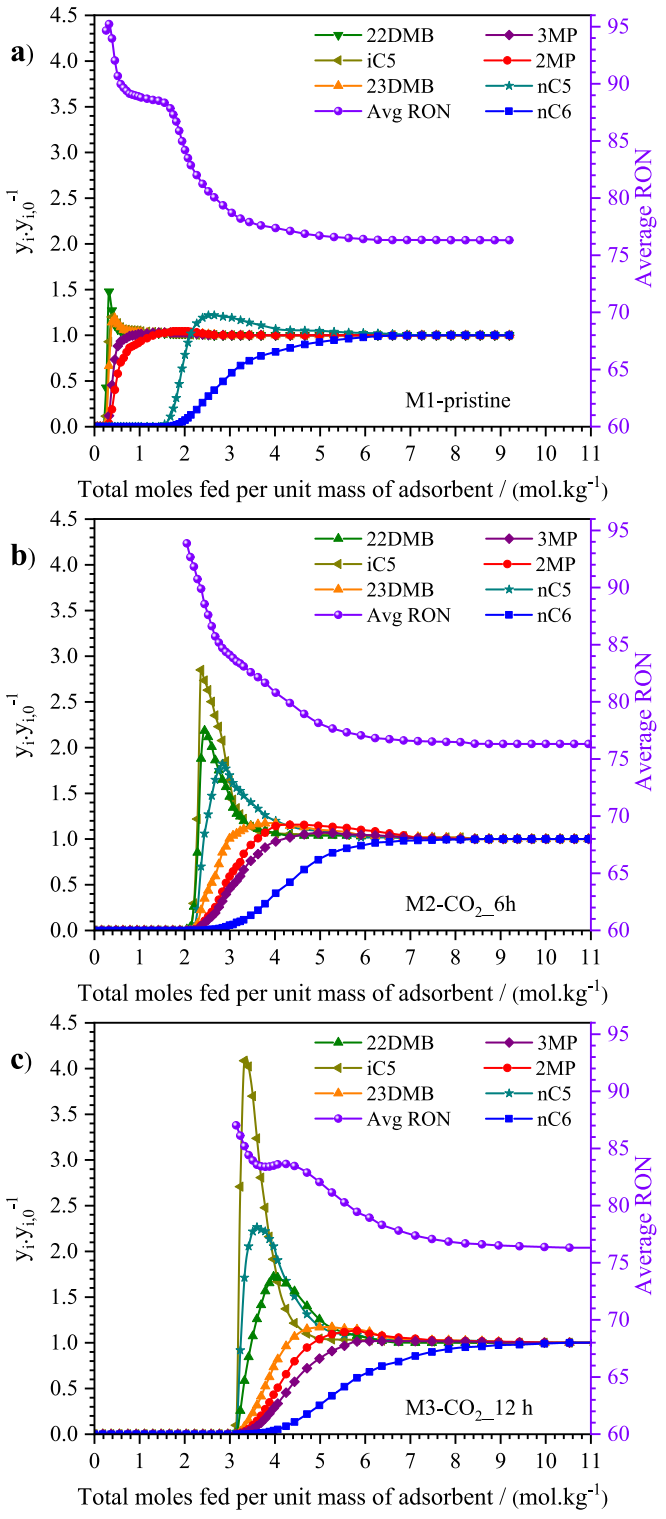

Fig. 4. Experimental breakthrough curves for a septenary equimolar mixture of C5 and C6 alkane isomers in 3D-printed monoliths at 373 K and 50.0 kPa: a) M1-pristine, b) M2-CO_2_6h, and c) M3-CO_2_12h.

by M1-pristine (0.86 mol.kg^{-1}) is around three and four times lower than the ones obtained in M2-CO_2_6h (2.24 mol.kg^{-1}) and M3-CO_2_12h (3.20 mol.kg^{-1}), respectively. This trend can be extended to the whole range of experimental conditions studied. These experimental findings are consistent with the characterization data reported in Table 1, such as S_{BET}, S_{QSDFT}, and cumulative pore volume, which increases according to the degree of CO_2 activation. Moreover, according to Steldinger [34], despite creating additional microporosity, in the CO_2 activation process, there are also pore widening and joining of close pores (caused by the removal of the separating walls between them due to mass loss). These effects are more pronounced as temperature and/or activation time increases. The oxidation and, thus, widening of the pore mouths is very likely the main reason for the loss of molecular sieving properties for M2-CO_2_6h and M3-CO_2_12h compared to non-activated M1-pristine. Although much higher loadings were obtained in the CO_2-activated monoliths, their selectivities (around 0.58, Table S6, Supplementary Data), calculated by the ratio of the loadings between linear over branched alkanes (Eq. S2, Supplementary Data), are considerably lower (around five times) than that of M1-pristine (3.26).

It is evident from the breakthrough experimental data that the monolith M1-pristine is the most suitable material for C5/C6 alkane isomer separation into fractions of linear and branched ones. Accordingly, the effect of temperature and total alkane partial pressure is provided in the following sections. More information about the experimental breakthrough curves performed in M2-CO_2_6h and M3-CO_2_12h is given in Figs. S3–S6 (Supplementary Data).

4.3. Effect of temperature and total alkane pressure on the multicomponent adsorption of C5 and C6 alkane isomers in M1-pristine

Figs. 5, 6, and 7 show the breakthrough curves for the temperatures of 373, 423, and 473 K in M1-pristine, respectively, plotted in terms of the normalized molar fraction ratio of each alkane isomer as a function of time. In each figure, the effect of total alkane partial pressure in the feed is shown: a) 10 kPa, b) 25 kPa, and c) 50 kPa. The real-time RON of the product mixture leaving the column is also illustrated. The results indicate that the size-selective separation of linear/branched alkanes is kept for the entire range of working conditions.

Regarding the adsorption of linear alkanes, despite having the same kinetic diameter (0.43 nm), the nC6 is preferentially adsorbed over the nC5, probably due to its longer linear chain that maximizes the contact surface area with the pore walls of the monolith. Their equilibrium competition for sorption can result in a feed concentration rising to 30% for the nC5. Additionally, the temperature does not strongly affect qualitatively the shape of the breakthrough curves since a similar picture is observed. At a fixed total alkane pressure, the mass transfer zone width for nC5 and nC6 also remains nearly constant, as well as the magnitude of the roll-up for nC5. Likewise, the plateau, corresponding to a RON value of 89, is practically the same, especially at 373 and 423 K.

Regarding the adsorption loadings, it can be seen that at the working condition of 373 K and 50 kPa, the total loading is 0.86 mol.kg^{-1} (please see Table S6), which in terms of the mass of alkanes adsorbed per mass of monolith (g.100g$_{ads}^{-1}$), corresponds to around 7.4 wt%. Accordingly, this value compares to the ones observed in the reference material zeolite 5A operating in similar conditions [41,42], being the maximum loading of alkanes in zeolite 5A around 13 wt%. However, in industrially working conditions, it is difficult to operate under this loading with zeolite 5A due to its highly rectangular isotherm, a major drawback for the regeneration steps in cyclic operation [41–44]. Therefore, the experimental findings from this work reveal that the 3D-printed material can be a potential adsorbent for designing improved separation processes of linear/branched light alkanes. Section S3 and Table S7 (Supplementary Data) briefly overview the features of other works using carbon-based materials for the C5/C6 alkane isomer separation.

The sorption selectivities values, reported in Table S6 (Supplementary Data), are plotted as a function of total alkane partial pressure in Fig. 8. They slightly decrease with increasing temperature, ranging from around 3.7 at 373 K to 2.5 at 473 K. Moreover, they remain practically constant in the range of total alkane partial pressure studied.

The corresponding septenary adsorption equilibrium isotherms of C5 and C6 isomers in M1-pristine are shown in Fig. 9. The significant difference between linear and branched alkanes loadings is clearly

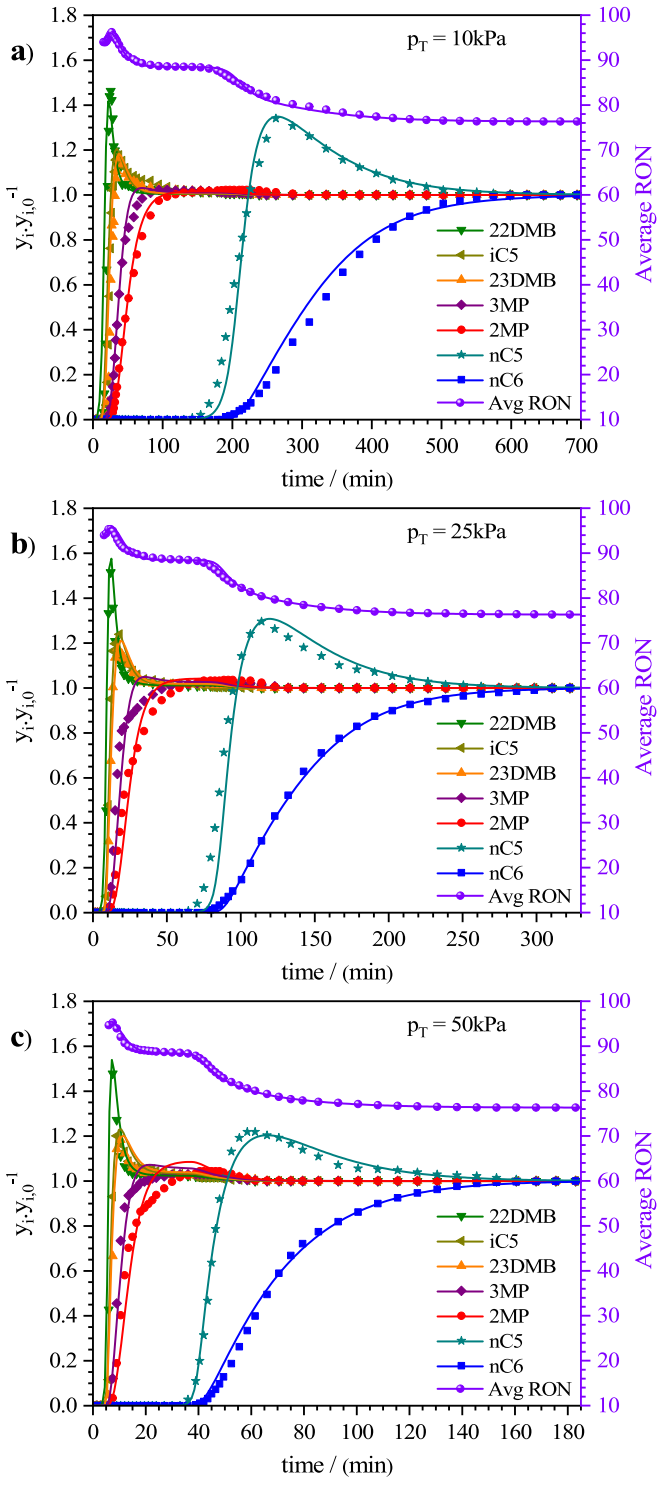

Fig. 5. Experimental and numerical breakthrough curves for a septenary equimolar mixture of C5 and C6 alkane isomers in M1-pristine at 373 K: a) 10 kPa, b) 25 kPa, and c) 50 kPa. The continuous lines represent the numerical simulations.

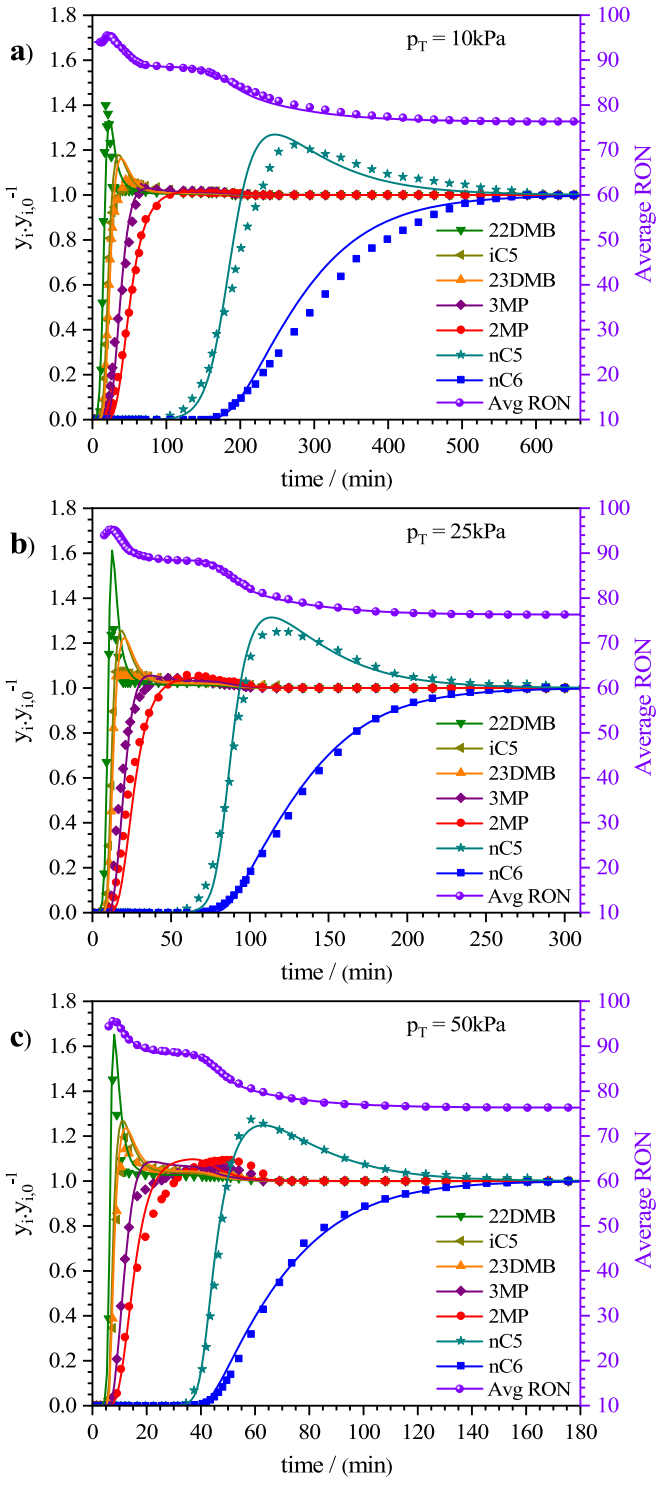

Fig. 6. Experimental and numerical breakthrough curves for a septenary equimolar mixture of C5 and C6 alkane isomers in M1-pristine at 423 K: a) 10 kPa, b) 25 kPa, and c) 50 kPa. The continuous lines represent the numerical simulations.

observed. Also, whatever the temperature studied, the isotherms are marked as type I according to the IUPAC classification, typical of adsorption in micropores [37].

4.4. Modeling and simulation of dynamic breakthrough curves in M1-pristine

Modeling adsorption data is of fundamental importance for the proper design/prediction of cyclic adsorption processes. The fitting of the multicomponent breakthrough curves in M1-pristine is shown in Figs. 5–7 by the continuous lines, predicted by the dynamic fixed bed

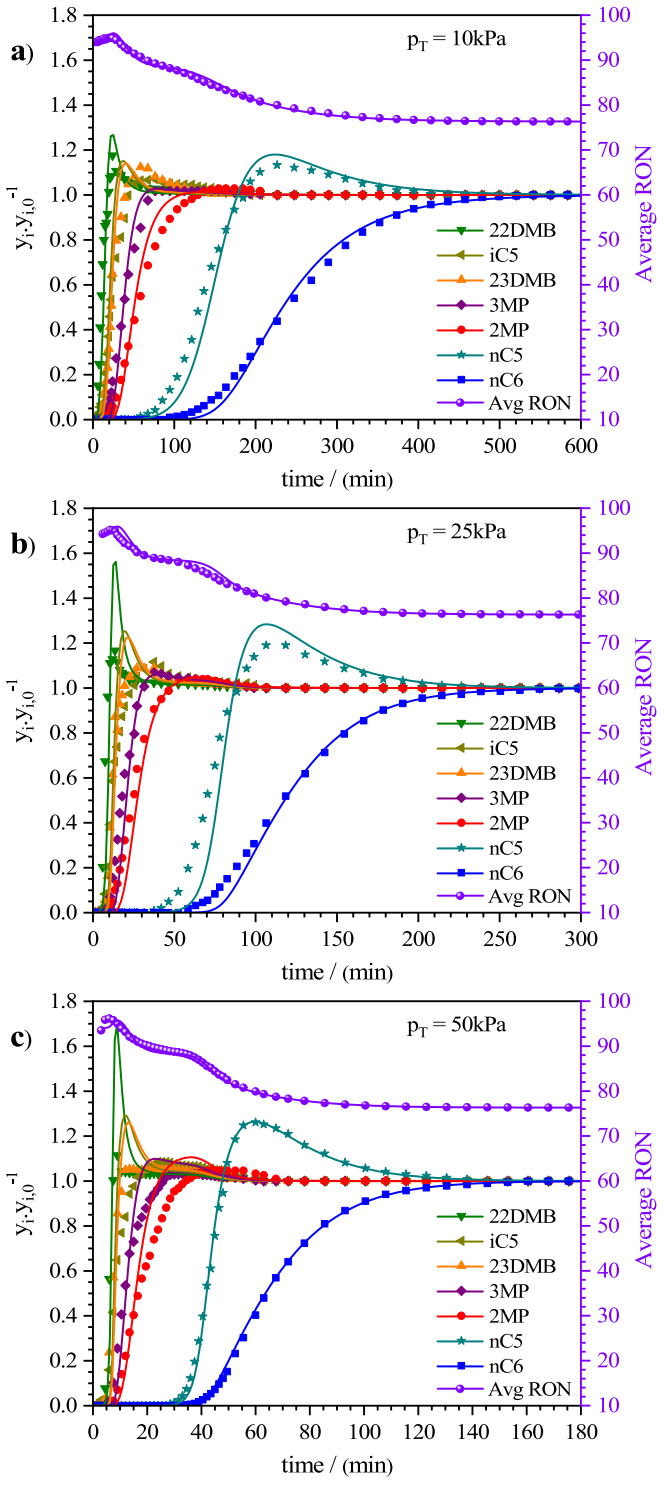

Fig. 7. Experimental and numerical breakthrough curves for a septenary equimolar mixture of C5 and C6 alkane isomers in M1-pristine at 473 K: a) 10 kPa, b) 25 kPa, and c) 50 kPa. The continuous lines represent the numerical simulations.

adsorption model described in Section S2 (Supplementary Data). For the respective fitting, it was necessary to set up convenient adsorption equilibrium and mass transfer models.

The equilibrium data (Table S6, Supplementary Data) was correlated with a semi-empirical heterogeneous patchwise adsorption model with two different patches, acting independently [45]: i) one where only the linear alkanes are adsorbed following an extended Langmuir isotherm;

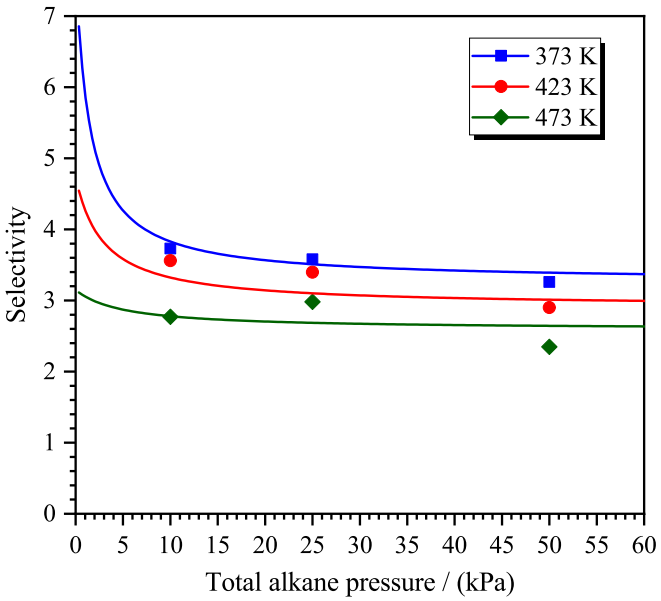

Fig. 8. Sorption selectivities of C5 and C6 alkane isomers in M1-pristine. The continuous lines represent model predictions.

ii) the other where only the branched alkanes are adsorbed, also following an extended Langmuir isotherm (Eq. S9, Supplementary Data). The corresponding model parameters are reported in Table S8 (Supplementary Data). The saturation loading capacities, q_{sat}, for the adsorption of linear alkanes in the respective patch was allowed to be temperature-dependent, in which we assumed that the effect of temperature is the same, being δ equal to 0.87. Regarding the adsorption heats, $-\Delta H$, they range around 18.2 and 8.5 kJ.mol^{-1} for the linear and branched alkanes, respectively. The continuous lines shown in Fig. 8 clearly validate this semi-empirical model for the sorption of C5/C6 alkane isomers in M1-pristine.

Concerning mass transfer, as mentioned earlier, the sorption dynamics of linear and branched alkanes occur under different conditions in M1-pristine. While the branched molecules can quickly fill the small portion of larger pores accessible to all species, resulting in sharp breakthrough curves, the adsorption of linear molecules takes place on the narrow pores, imposing diffusional limitations, ultimately resulting in more "diffuse" breakthrough curves. Therefore, the numerical simulations were conducted by adjusting two independent mass transfer coefficients (Eq. S8, Table S2, Supplementary Data): one accounting for the overall sorption of linear alkanes ($k_{LDF,l}$) and the other for the sorption of branched alkanes ($k_{LDF,b}$). The k_{LDF} coefficients found by trial and error to obtain the best fit of the experimental data range from 0.0018 s^{-1} (373 K) to 0.0031 s^{-1} (473 K) for nC5/nC6 and from 0.018 s^{-1} (373 K) to 0.031 s^{-1} (473 K) for their branched counterparts. Their temperature dependence, which follows the Arrhenius equation (Eq. S8, Table S2, Supplementary Data), gave rise to an activation energy, ΔE_i, of 8.0 kJ.mol^{-1}. As it shows, the $k_{LDF,l}$ is one order of magnitude lower than $k_{LDF,b}$, which seems fair considering the diffusional effects arising from the microporous morphology and connectivity of M1-pristine.

It is evident that the numerical predictions are in good agreement with experimental data for the range of working conditions covered. The profiles of the breakthrough curves were properly fitted, being the width of the mass-transfer zone and the roll-up due to competitive adsorption conveniently predicted in most cases. These results indicate that the empirical patchwise adsorption model, combined with a simple lumped kinetic mass transfer rate model, is adequate to comprehensively analyze the sorption phenomena of C5/C6 alkane isomers in the 3D-printed monolith. All the model parameters used for simulating the experimental multicomponent breakthrough curves are reported in

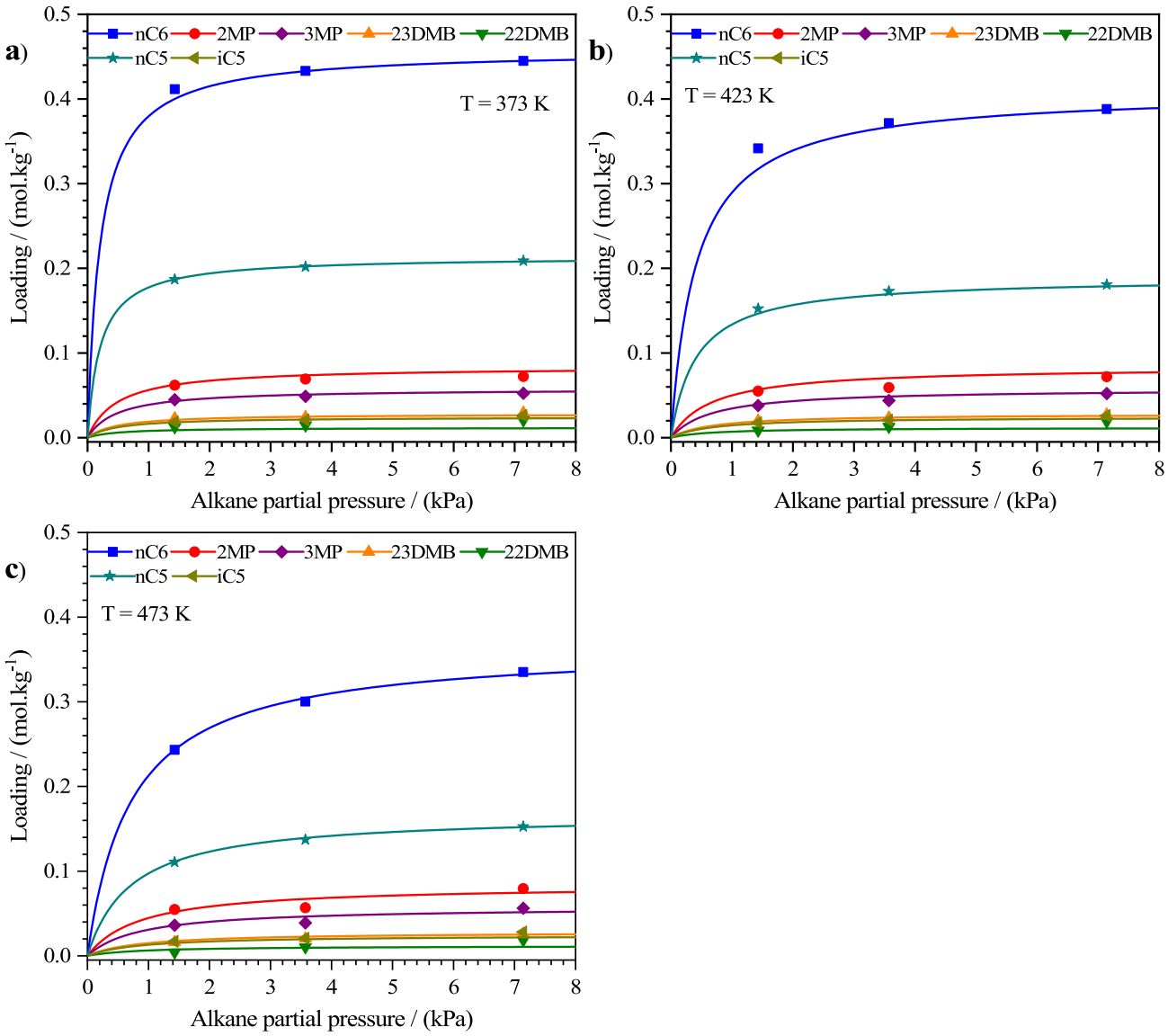

Fig. 9. Septenary adsorption equilibrium isotherms of C5 and C6 alkane isomers in M1-pristine: a) 373 K, b) 423 K, and c) 473 K. The continuous lines represent model predictions.

Tables S9 – S11 (Supplementary Data).

5. Conclusions

We report the first experimental study on the sorption of C5 and C6 alkane isomers on a series of hierarchically structured 3D-printed porous carbons monoliths. Multicomponent breakthrough experiments with septenary feed mixtures disclose that the non-activated monolith, M1-pristine, can completely separate linear (nC6/nC5) from their branched isomers (2MP/3MP/23DMB/iC5/22DMB – barely adsorbed), in a broad range of working conditions, through a near molecular sieving effect arising from its micropore morphology and connectivity. Remarkably, this separation performance, similar to the one observed in the benchmark zeolite 5A, establishes the feasibility of the emerging 3D-printed carbon monoliths for their potential application in the industrial sector. The adsorption equilibrium data of the alkanes in M1-pristine was conveniently correlated with a semi-empirical patchwise model (two patches), and the breakthrough curves suitable predicted by a dynamic fixed bed adsorption model.

The breakthrough experiments performed in the activated monoliths at 1133 K, M2-CO_2_6h, and M3-CO_2_12h, exhibited a much larger sorption capacity. All alkanes were adsorbed with a hierarchy order following the normal boiling point order of the compounds: nC6 > 3MP > 2MP > 23DMB > 22DMB > nC5 > iC5. Consequently, mixture loadings around three and four times higher than those from M1-pristine were obtained in monoliths M2-CO_2_6h and M3-CO_2_12h, respectively.

Based on the outcomes from this work and concerning potential strategies for octane number enhancement in TIP processes, as well as other challenging separation tasks, it would be worth performing further studies regarding the stage of CO_2 activation in the production of 3D-printed monoliths. An interesting idea might be to find such a combination of temperature and time to possibly increase the specific surface area by adding a new fraction of micropores without provoking significant pore widening (monoliths M2-CO_2_6h and M3-CO_2_12h), focusing on enhancing the adsorption capacity of linear alkanes. Finally, this work provides an important reference for the utilization of structured materials in this field of alkanes separation, besides opening a new frontier for the use of carbon-based materials.

CRediT authorship contribution statement

Adriano Henrique: Writing – original draft, Writing – review &

editing, Software, Validation, Investigation, Formal analysis. **Hendryk Steldinger:** Writing – review & editing, Software, Validation, Investigation, Formal analysis. **Jose L. Diaz de Tuesta:** Writing – review & editing, Validation, Project administration, Funding acquisition. **Jan Gläsel:** Writing – review & editing, Software, Validation, Investigation, Formal analysis. **Alírio E. Rodrigues:** Writing – review & editing, Visualization, Validation, Supervision, Project administration, Funding acquisition. **Helder T. Gomes:** Writing – review & editing, Visualization, Validation, Supervision, Resources, Project administration, Funding acquisition. **Bastian J.M. Etzold:** Writing – review & editing, Visualization, Validation, Supervision, Resources, Project administration, Funding acquisition. **José A.C. Silva:** Writing – review & editing, Visualization, Validation, Supervision, Resources, Project administration, Funding acquisition.

Declaration of Competing Interest

The authors declare that they have no known competing financial interests or personal relationships that could have appeared to influence the work reported in this paper.

Data availability

Data will be made available on request.

Acknowledgments

The authors acknowledge financial support from: (1) project POCI01-0145-FEDER-016517 (PTDC/QEQ-PRS/3599/2014) funded by FEDER funds through COMPETE2020 and Fundação para a Ciência e a Tecnologia (FCT); (2) Project PTDC/EQU-EPQ/0467/2020; (3) FCT PhD scholarship to Adriano Henrique (SFRH/BD/148525/2019); (4) Joint financial support from FCT (Portugal) and DAAD (Germany); (5) National funds FCT/MCTES (PIDDAC) to CIMO (UIDB/00690/2020 and UIDP/00690/2020), SusTEC (LA/P/0007/2021), LSRE-LCM (UIDB/50020/2020 and UIDP/50020/2020), and ALiCE (LA/P/0045/2020). Jose L. Diaz De Tuesta acknowledges the financial support through the program of Atracción al Talento of Comunidad de Madrid (Spain) for the individual research grants 2020-T2/AMB-19836 and 2022-T1/AMB-23946.

The authors also acknowledge Dr. M. Rückriem and Dr. A. Schreiber from Microtrac Retsch GmbH for their kind support with nitrogen physisorption measurements.

Appendix A. Supplementary data

Supplementary data to this article can be found online at https://doi.org/10.1016/j.cej.2023.145138.

References

[1] J. Jänchen, K. Schumann, E. Thrun, A. Brandt, B. Unger, U. Hellwig, Preparation, hydrothermal stability and thermal adsorption storage properties of binderless zeolite beads, Int. J. Low-Carbon Technol. 7 (2012) 275–279, https://doi.org/10.1093/ijlct/cts037.

[2] L. Yu, J. Gong, C. Zeng, L. Zhang, Synthesis of binderless zeolite X microspheres and their CO2 adsorption properties, Sep. Purif. Technol. 118 (2013) 188–195, https://doi.org/10.1016/j.seppur.2013.06.035.

[3] K. Gleichmann, B. Unger, A. Brandt, Zeolites - Useful Minerals, InTech, 2016.

[4] A. Permyakova, O. Skrylnyk, E. Courbon, M. Affram, S. Wang, U.H. Lee, A. H. Valekar, F. Nouar, G. Mouchaham, T. Devic, G. De Weireld, J.S. Chang, N. Steunou, M. Frère, C. Serre, Synthesis optimization, shaping, and heat reallocation evaluation of the hydrophilic metal–organic framework MIL-160(Al), ChemSusChem 10 (2017) 1419–1426, https://doi.org/10.1002/cssc.201700164.

[5] A.H. Valekar, S.G. Lee, K.H. Cho, U.H. Lee, J.S. Lee, J.W. Yoon, Y.K. Hwang, S. J. Cho, J.S. Chang, Shaping of porous metal-organic framework granules using mesoporous ρ-alumina as a binder, RSC Adv. 7 (2017) 55767–55777, https://doi.org/10.1039/c7ra11764g.

[6] Y. Khabzina, J. Dhainaut, M. Ahlhelm, H.J. Richter, H. Reinsch, N. Stock, D. Farrusseng, Synthesis and shaping scale-up study of functionalized UiO-66 MOF for ammonia air purification filters, Ind. Eng. Chem. Res. 57 (2018) 8200–8208, https://doi.org/10.1021/acs.iecr.8b00808.

[7] A. Mallick, G. Mouchaham, P.M. Bhatt, W. Liang, Y. Belmabkhout, K. Adil, A. Jamal, M. Eddaoudi, Advances in shaping of metal-organic frameworks for CO2 capture: understanding the effect of rubbery and glassy polymeric binders, Ind. Eng. Chem. Res. 57 (2018) 16897–16902, https://doi.org/10.1021/acs.iecr.8b03937.

[8] P.D.A. McCrae, T. Zhang, D.R.B. Walker, Method of Making Shaped Activated Carbon. U.S. Patent 20030022787A1, 2003.

[9] X. Shao, Z. Feng, R. Xue, C. Ma, W. Wang, X. Peng, D. Cao, Adsorption of CO2, CH4, CO2/N2 and CO2/CH4 in novel activated carbon beads: preparation, measurements and simulation, AIChE J 57 (2011) 3042–3051, https://doi.org/10.1002/aic.12515.

[10] N. Sun, C. Sun, H. Liu, J. Liu, L. Stevens, T. Drage, C.E. Snape, K. Li, W. Wei, Y. Sun, Synthesis, characterization and evaluation of activated spherical carbon materials for CO2 capture, Fuel 113 (2013) 854–862, https://doi.org/10.1016/j.fuel.2013.03.047.

[11] F. Rezaei, P. Webley, Optimum structured adsorbents for gas separation processes, Chem. Eng. Sci. 64 (2009) 5182–5191, https://doi.org/10.1016/j.ces.2009.08.029.

[12] F. Rezaei, P. Webley, Structured adsorbents in gas separation processes, Sep. Purif. Technol. 70 (2010) 243–256, https://doi.org/10.1016/j.seppur.2009.10.004.

[13] S. Govender, H.B. Friedrich, Monoliths: a review of the basics, preparation methods and their relevance to oxidation, Catalysts 7 (2017) 62, https://doi.org/10.3390/catal7020062.

[14] H. Thakkar, S. Eastman, A. Hajari, A.A. Rownaghi, J.C. Knox, F. Rezaei, 3D-Printed zeolite monoliths for CO2 removal from enclosed environments, ACS Appl. Mater. Interfaces 8 (2016) 27753–27761, https://doi.org/10.1021/acsami.6b09647.

[15] S. Lawson, X. Li, H. Thakkar, A.A. Rownaghi, F. Rezaei, Recent advances in 3D printing of structured materials for adsorption and catalysis applications, Chem. Rev. 121 (2021) 6246–6291, https://doi.org/10.1021/acs.chemrev.1c00060.

[16] A. Jandyal, I. Chaturvedi, I. Wazir, A. Raina, M.I. Ul Haq, 3D printing – a review of processes, materials and applications in industry 4.0, Sustain. Oper. Comput. 3 (2022) 33–42, https://doi.org/10.1016/j.susoc.2021.09.004.

[17] H. Thakkar, S. Eastman, A. Al-Mamoori, A. Hajari, A.A. Rownaghi, F. Rezaei, Formulation of aminosilica adsorbents into 3D-printed monoliths and evaluation of their CO2 capture performance, ACS Appl. Mater. Interfaces 9 (2017) 7489–7498, https://doi.org/10.1021/acsami.6b16732.

[18] S. Couck, J. Lefevere, S. Mullens, L. Protasova, V. Meynen, G. Desmet, G.V. Baron, J.F.M. Denayer, CO2, CH4 and N2 separation with a 3DFD-printed ZSM-5 monolith, Chem. Eng. J. 308 (2017) 719–726.

[19] S. Couck, J. Cousin-Saint-Remi, S. Van der Perre, G.V. Baron, C. Minas, P. Ruch, J. F.M. Denayer, 3D-printed SAPO-34 monoliths for gas separation, Microporous Mesoporous Mater. 255 (2018) 185–191.

[20] H. Thakkar, S. Lawson, A.A. Rownaghi, F. Rezaei, Development of 3D-printed polymer-zeolite composite monoliths for gas separation, Chem. Eng. J. 348 (2018) 109–116, https://doi.org/10.1016/j.cej.2018.04.178.

[21] H. Thakkar, S. Eastman, Q. Al-Naddaf, A.A. Rownaghi, F. Rezaei, 3D-Printed metal-organic framework monoliths for gas adsorption processes, ACS Appl. Mater. Interfaces 9 (2017) 35908–35916, https://doi.org/10.1021/acsami.7b11626.

[22] S. Lawson, F. Rezaei, Effects of process parameters on CO2/H2 separation performance of 3D-printed MOF-74 monoliths, ACS Sustain. Chem. Eng. 9 (2021) 10902–10912, https://doi.org/10.1021/acssuschemeng.1c03443.

[23] S. Lawson, Q. Al-Naddaf, A. Krishnamurthy, M.S. Amour, C. Griffin, A. A. Rownaghi, J.C. Knox, F. Rezaei, UTSA-16 growth within 3D-printed Co-kaolin monoliths with high selectivity for CO2/CH4, CO2/N2, and CO2/H2 separation, ACS Appl. Mater. Interfaces 10 (2018) 19076–19086, https://doi.org/10.1021/acsami.8b05192.

[24] C.A. Grande, R. Blom, V. Middelkoop, D. Matras, A. Vamvakeros, S.D.M. Jacques, A.M. Beale, M. di Michiel, K. Anne Andreassen, A.M. Bouzga, Multiscale investigation of adsorption properties of novel 3D printed UTSA-16 structures, Chem. Eng. J. 402 (2020), 126166, https://doi.org/10.1016/j.cej.2020.126166.

[25] S. Lawson, C. Griffin, K. Rapp, A.A. Rownaghi, F. Rezaei, Amine-functionalized MIL-101 monoliths for CO2 removal from enclosed environments, Energy Fuel 33 (2019) 2399–2407, https://doi.org/10.1021/acs.energyfuels.8b04508.

[26] S. Lawson, M. Snarzyk, D. Hanify, A.A. Rownaghi, F. Rezaei, Development of 3D-printed polymer-MOF monoliths for CO2 adsorption, Ind. Eng. Chem. Res. 59 (2020) 7151–7160, https://doi.org/10.1021/acs.iecr.9b05445.

[27] S. Lawson, Q. Al-Naddaf, K. Newport, A. Rownaghi, F. Rezaei, Assessment of CO2/CH4 separation performance of 3D-printed carbon monoliths in pressure swing adsorption, Ind. Eng. Chem. Res. 60 (2021) 16445–16456, https://doi.org/10.1021/acs.iecr.1c01741.

[28] M.J. Regufe, A.F.P. Ferreira, J.M. Loureiro, A. Rodrigues, A.M. Ribeiro, Electrical conductive 3D-printed monolith adsorbent for CO2 capture, Microporous Mesoporous Mater. 278 (2019) 403–413, https://doi.org/10.1016/j.micromeso.2019.01.009.

[29] D.N.D.L. Mendes, A. Gaspar, I. Ferreira, J.P.B. Mota, R.P.P.L. Ribeiro, 3D-printed hybrid zeolitic/carbonaceous electrically conductive adsorbent structures, Chem. Eng. Res. Des. 174 (2021) 442–453, https://doi.org/10.1016/j.cherd.2021.08.020.

[30] S.A. Treese, P.R. Pujadó, D.S.J. Jones (Eds.), Handbook of Petroleum Processing, Springer International Publishing, Cham, 2015.

[31] T.C. Holcombe, Total Isomerization Process, US 4,210,771, 1980.

[32] R.A. Meyers, Handbook of petroleum refining processes, 3rd Ed.,, McGraw-Hill Education, 2004.

[33] H. Steldinger, A. Esposito, K. Brunnengräber, J. Gläsel, B.J.M. Etzold, Activated carbon in the third dimension—3D printing of a tuned porous carbon, Adv. Sci. 6 (2019) 1901340, https://doi.org/10.1002/advs.201901340.
[34] H. Steldinger, 3D printing of Activated Carbon and Exemplary Application as Adsorbent in the Electric Swing Adsorption, Technische Universität Darmstadt, 2020. PhD Thesis.
[35] A. Henrique, A.E. Rodrigues, J.A.C. Silva, Separation of hexane isomers in ZIF-8 by fixed bed adsorption, Ind. Eng. Chem. Res. 58 (2019) 378–394, https://doi.org/10.1021/acs.iecr.8b05126.
[36] P.F. Brântuas, A. Henrique, M. Wahiduzzaman, A. Von Wedelstedt, T. Maity, A. Rodrigues, F. Nouar, U.-H. Lee, K.H. Cho, G. Maurin, J.A.C. Silva, C. Serre, Separation of branched alkane feeds by a synergistic action of zeolite and metal-organic framework, Adv. Sci. (2022) 2201494, https://doi.org/10.1002/advs.202201494.
[37] M. Thommes, K. Kaneko, A.V. Neimark, J.P. Olivier, F. Rodriguez-Reinoso, J. Rouquerol, K.S.W. Sing, Physisorption of gases, with special reference to the evaluation of surface area and pore size distribution (IUPAC technical report), Pure Appl. Chem. 87 (2015) 1051–1069, https://doi.org/10.1515/pac-2014-1117.
[38] Bulk Density of Activated Carbon. https://www.allcarbon.net/bulk-density-of-activated-carbon/ (accessed July 24, 2023).
[39] Molecular Sieves. https://www.pataliachem.net/molecular-sieve.html (accessed July 24, 2023).
[40] J. Jeromenok, J. Weber, Restricted access: on the nature of adsorption/desorption hysteresis in amorphous, microporous polymeric materials, Langmuir 29 (2013) 12982–12989, https://doi.org/10.1021/la402630s.
[41] J.A.C. Silva, A.E. Rodriguez, Sorption and diffusion of n-pentane in pellets of 5a zeolite, Ind. Eng. Chem. Res. 36 (1997) 493–500, https://doi.org/10.1021/ie960477c.
[42] J.A.C. Silva, A.E. Rodrigues, Equilibrium and kinetics of n-hexane sorption in pellets of 5a zeolite, AIChE J 43 (1997) 2524–2534, https://doi.org/10.1002/aic.690431014.
[43] J.A.C. Silva, A.E. Rodrigues, Separation of n/iso-paraffins mixtures by pressure swing adsorption, Sep. Purif. Technol. 13 (1998) 195–208, https://doi.org/10.1016/S1383-5866(98)00043-4.
[44] J.A.C. Silva, F.A. Da Silva, A.E. Rodrigues, Separation of n/iso paraffins by PSA, Sep. Purif. Technol. 20 (2000) 97–110, https://doi.org/10.1016/S1383-5866(00)00064-2.
[45] D.D. Do, Adsorption Analysis: Equilibria and Kinetics, Imperial College Press, 1998.